X-raying extragalactic gas: warm-hot gas in the EAGLE simulations

Wijers, N.A.

5

Comparing EAGLE simulation predictions to X-ray absorption line observations

Based on contributions to:

F. Nicastro, J. Kaastra, Y. Krongold, S. Borgani, E. Branchini, R. Cen, M. Dadina, C. W. Danforth, M. Elvis, F. Fiore, A. Gupta, S. Mathur, D. Mayya, F. Paerels, L. Piro, D. Rosa-Gonzalez, J. Schaye, J. M. Shull, J. Torres-Zafra, N. Wijers, & L. Zappacosta. *Observations of the missing baryons in the warm–hot intergalactic medium.*
2018, Nature, 558, 406–409

Sean D. Johnson, John S. Mulchaey, Hsiao-Wen Chen, Nastasha A. Wijers, Thomas Connor, Sowgat Muzahid, Joop Schaye, Renyue Cen, Scott G. Carlsten, Jane Charlton, Maria R. Drout, Andy D. Goulding, Terese T. Hansen, & Gregory L. Walth. *The Physical Origins of the Identified and Still Missing Components of the Warm-Hot Intergalactic Medium: Insights from Deep Surveys in the Field of Blazar 1ES1553+113.*
2019, ApJ, 884, L31

Jussi Ahoranta, Jukka Nevalainen, Nastasha Wijers, Alexis Finoguenov, Massimiliano Bonamente, Elmo Tempel, Evan Tilton, Joop Schaye, Jelle Kaastra, & Ghassem Gozaliasl. *Hot WHIM counterparts of FUV O VI absorbers: Evidence in the line-of-sight towards quasar 3C 273.*
2020, A&A, 634, A106

Jussi Ahoranta, Alexis Finoguenov, Massimiliano Bonamente, Evan Tilton, Nastasha Wijers, Sowgat Muzahid, & Joop Schaye. *Discovery of a multi–phase O VI and O VII absorber in the circumgalactic/intergalactic transition region.*
2021, submitted to A&A

Abstract

We examine a number of recent comparisons between claimed detections of extragalactic soft X-ray line absorbers and predictions from the EAGLE simulations. These lines are expected to be sensitive to the warm-hot phases of the intergalactic medium and the gaseous haloes of galaxies. Generally, EAGLE seems to be consistent with these observations. However, the comparisons remain difficult. This is due to the small number of detected systems, and the strong selection effects imposed by the limits of currently available instruments. We find a hint that the strong soft X-ray absorbers studied may be too concentrated around galaxies in EAGLE, but this is very uncertain. The simulation has proven useful in verifying the reasonability of assumptions made in the modelling and interpretation of the absorption data, such as whether different ions are expected to trace the same gas phase, or how rare we think strong absorbers would be, far from any detected galaxies. The simulation can also be used to test whether a claimed detection is physically reasonable.

5.1 Introduction

Much is still unknown about the warm-hot intergalactic medium (WHIM) and the warm/hot phase of the circumgalactic medium (CGM). The intra-group medium (IGrM) and intra-cluster medium (ICM) have been detected in X-ray emission (see, e.g., the review by Werner & Mernier 2020). This has been used to constrain a number of ICM properties, such as the electron density, temperature, and metallicity of the hot gas. Additionally, ICM turbulence has been constrained in different ways (e.g., Hitomi Collaboration et al. 2018; Zhuravleva et al. 2014). Some observations of X-ray emission around lower-mass ($M_\star \approx 10^{11}\,M_\odot$), spiral galaxies exist. Many of these observations are limited to the close environment of the central galaxy (e.g., Bogdán et al. 2015), though observations of the more extended CGM exist (Das et al. 2020).

For the CGM, around lower-mass galaxies, and at low redshift, $z < 1$, most of what we know comes from far ultraviolet (FUV) absorption lines, especially from surveys with the *Cosmic Origins Spectrograph* on the *Hubble Space Telescope* (HST-COS) (e.g., Tumlinson et al. 2011; Johnson et al. 2015, 2017). The ions producing these absorption lines mainly arise in $\sim 10^4$–$10^{5.5}$ K gas (e.g., Tumlinson et al. 2017, fig. 6). However, at halo masses $M_{200c} \gtrsim 10^{11.5}$–$10^{12}\,M_\odot$, we expect much of the CGM to consist of a virialized, warm-hot, volume-filling phase (e.g., Dekel & Birnboim 2006; Kereš et al. 2009; Van de Voort et al. 2011; Correa et al. 2018), with much of its gas at temperatures $\gtrsim 10^{5.5}$–10^6 K (e.g., Chapter 3; Wijers et al. 2020).

The warm-hot phase, at $\sim 10^{5.5}$–10^7 K, has been more difficult to detect. In the observational census of baryons at low redshift by Shull et al. (2012), some mass was still missing. The census included galaxies, cool and warm ($\lesssim 10^6$ K) IGM, ICM, IGrM, and an uncertain CGM component. The expected baryon density comes from measurements of the cosmic microwave background (CMB; e.g., Planck Collaboration et al. 2014) and big bang nucleosynthesis (e.g., the review by Cyburt et al. 2016). In cosmological, hydrodynamical simulations, the low-redshift 'missing baryons' are in the warm-hot, diffuse phase, forming the WHIM (e.g., Hellsten et al. 1998; Cen & Ostriker 1999) and the warm-hot phase of the CGM.

Recently, Macquart et al. (2020) did detect a baryon density consistent with CMB measurements using the dispersion measures of fast radios bursts (FRBs). However, due to the small number of sightlines, combined with uncertainties about the dispersion measure contributions of the Milky Way (halo) and the FRB host galaxies, the range of allowed baryon density values is still large. FRB dispersion measures are only sensitive to the (total) column density of electrons along a line of sight. This means that they can be useful in constraining the distribution of gas in the CGM and IGM (e.g., McQuinn 2014; Ravi 2019; Walters et al. 2019), but these measurements are not sensitive to e.g., the metallicity of the gas, or the temperature of diffuse gas. This is because hydrogen in the IGM is almost fully (photo-)ionized, and dispersion measures are not sensitive to the difference between cool, photo-ionized and warm/hot, collisionally ionized gas.

The Sunyaev-Zel'dovich (SZ) effect has also been used to measure warm-hot gas, in massive filaments, CGM, IGrM and ICM. Studies of clusters (e.g., the review by Mroczkowski et al. 2019) and massive filaments (e.g., de Graaff et al. 2019; Tanimura et al. 2019) have used the thermal SZ (tSZ) effect, which is determined by the total pressure along a line of sight. To find the massive filaments, pairs of massive galaxies were stacked. This yielded detections of the massive filaments between the pairs of galaxies. The haloes of lower-mass galaxies (CGM and IGrM) were detected using a combination of data. Lim et al. (2018) studied the IGrM ($M_{500c} \geq 10^{12}\,M_\odot$) using the tSZ effect, and known positions of galaxy groups. In ad-

dition to tSZ data, Lim et al. (2020) used measurements of the kinetic SZ (kSZ) effect, as well as the positions, masses, and peculiar velocities of haloes, to constrain the temperatures and gas masses of CGM, IGrM, and ICM. These peculiar velocities are important because the kSZ effect measures the electron momentum along the line of sight, meaning that with a known velocity, the kSZ effect is a measure of the (ionized) gas mass of the halo. It has been difficult to measure the SZ effect in the CGM of galaxies roughly the mass of the Milky Way due to the large beam size (spatial resolution) of the instruments (e.g., Mroczkowski et al. 2019).

Soft X-ray lines are also expected to be good probes of warm-hot ($T \sim 10^{5.5}$–10^{7} K) gas around or between galaxies (e.g., Perna & Loeb 1998; Hellsten et al. 1998; Chen et al. 2003; Cen & Fang 2006; Branchini et al. 2009). There have been various attempts to detect soft X-ray absorption lines against bright X-ray sources. Some of these have been blind searches, while others searched at specific, promising redshifts. This is a way to detect the warm-hot gas, and absorption lines also provide an avenue to measure, e.g., its temperature and density (e.g., Branchini et al. 2009).

These attempts have typically yielded low-significance measurements, or claimed discoveries that were later disputed. For example, in the spectrum of PKS 2155−304, Fang et al. (2002b) found an O VIII absorber using *Chandra* low energy transmission grating (LETG) data, at the same redshift as a small galaxy group and H I absorbers. The absorber had not been detected by Nicastro et al. (2002), who analysed *Chandra* LETG data of the same source. Rasmussen et al. (2003) and Cagnoni et al. (2004) also observed this source, with the *XMM-Newton* reflection grating spectrometer (RGS), and did not find evidence for this line. Nicastro et al. (2005) similarly found two combined O VII and N VII absorbers in the spectrum of Mrk 421, using ≈ 200 ks of *Chandra* LETG data. However, Kaastra et al. (2006) concluded that these detections were not statistically significant, due to the large number of redshift trials used in the blind search, and did not find evidence for these absorbers in *XMM-Newton* data of the same source.

Mathur et al. (2003) found three soft X-ray absorbers at 2–3σ significance, by searching for X-ray counterparts to six known O VI absorbers in the sightline to H1821+643. More recently, Bonamente et al. (2016) searched for soft X-ray absorption at specific redshifts where FUV absorbers had been found. They found likely O VIII absorption at the redshift of a broad Lyman α absorber using Chandra LETG observations. Kovács et al. (2019) found O VII absorption, attributed to the WHIM, by stacking data from different background sources and redshifts. They included 17 systems and redshifts where Lyman α had been detected near massive galaxies. Nicastro et al. (2017) review these searches for the WHIM.

Around the Milky Way, warm-hot gas has been detected in soft X-ray absorption and emission lines (e.g., Bregman & Lloyd-Davies 2007; Gupta et al. 2014; Miller & Bregman 2015; Das et al. 2019). The spatial extent of this gas is still uncertain (e.g., Bregman & Lloyd-Davies 2007; Gatuzz & Churazov 2018), although (Miller & Bregman 2015) did constrain this by fitting a model for the halo radial density profile to O VII and O VIII absorption and emission line measurements along many lines of sight. The detected emission and absorption lines have taught us much about the Milky Way CGM. From these lines, e.g., Kuntz & Snowden (2000) and Das et al. (2019) measured the temperature(s) of the warm/hot Milky Way CGM, e.g., Miller & Bregman (2015) measured its its density and metallicity, and Hodges-Kluck et al. (2016) measured its rotation . This illustrates the potential that extragalactic absorption line measurements have to constrain the properties of a larger diversity of galaxy haloes, and of the WHIM. However, the limited number of X-ray sightlines through these extragalactic systems will make it more difficult to constrain, e.g., their rotation, especially in individual systems.

We hope to learn more about the extragalactic warm/hot, virialized phase of the CGM, IGrM, and WHIM using soft X-ray absorption lines. However, with current instrumentation, only the strongest absorbers have been detectable, the number of observations is small, and many detections are of low statistical significance or disputed. Therefore, the extant comparisons to simulations are, for the most part, a sanity check of theoretical predictions, rather than a very stringent test.

On the other hand, the comparisons can provide a sanity check for uncertain detections. The theoretical predictions are valuable for checking the reasonability of assumptions made in the modelling of absorbers, such as whether different ions are expected to trace the same gas phase. With the increased sensitivity and spectral resolution of future missions, we hope to be able to test such assumptions instead, e.g., by comparing data on more transitions (absorption lines) than we can currently detect. This can provide stronger constraints on the conditions of the gas, such as its temperature. If sufficiently sensitive instruments are available, the combination of absorption and emission is also promising.

In this chapter, we will discuss comparisons of predictions from the EAGLE cosmological simulation to a few recently claimed detections of soft X-ray absorption lines tracing the WHIM or CGM. These are summaries of the EAGLE comparisons I contributed to different papers. First, we discuss blindly detected absorbers. In §5.3.1, we discuss a claim of two blind detections of O VII absorption in the spectrum of a very bright blazar (Nicastro et al. 2018). In §5.3.2, we discuss the further investigation of those absorbers by Johnson et al. (2019), which changed the interpretation of one of those absorbers, and cast doubt on the detection of the other. Next, we discuss soft X-ray absorbers found at the redshifts of two O VI absorbers. In §5.4.1, we discuss an O VIII and Ne IX absorber at one out of two investigated O VI redshifts (Ahoranta et al. 2020), and in 5.4.1, we discuss an O VII counterpart to the single O VI absorber in a sightline (Ahoranta et al. 2021).

When discussing distances, we indicate whether they are physical/proper (e.g., 'pkpc') or comoving (e.g., 'cMpc'). The exception are centimetres, which are always physical.

5.2 Methods

We used various results from EAGLE to compare its predictions to the different observational datasets. However, the basis for all the comparisons was the same: maps of ion column densities in EAGLE. In this section, we will give an overview of the EAGLE simulations, and explain how we produce these column density maps.

5.2.1 EAGLE

The EAGLE ('Evolution and Assembly of GaLaxies and their Environments'; Schaye et al. 2015; Crain et al. 2015; McAlpine et al. 2016) simulations are cosmological, hydrodynamical simulations. Gravitational forces are calculated using the GADGET-3 Tree-PM method (Springel 2005), and hydrodynamical forces are calculated using Smoothed Particle Hydrodynamics (SPH). Specifically, EAGLE uses the Anarchy implementation of SPH (Schaye et al. 2015, appendix A; Schaller et al. 2015). For the predictions in this chapter, we used the Ref-L100N1504 simulation. This is a simulated 100^3 cMpc^3 volume, with an (initial) gas mass resolution of $1.81 \times 10^6\,\mathrm{M}_\odot$ (Schaye et al. 2015). A ΛCDM cosmogony with cosmological parameters $\Omega_m = 0.307$, $\Omega_\Lambda = 0.693$, $\Omega_b = 0.04825$, $h = 0.6777$, $\sigma_8 = 0.8288$, $n_s = 0.9611$, and $Y = 0.248$ (Planck Collaboration et al. 2014) is assumed in EAGLE, and in the predictions we make from it.

Besides gravity and hydrodynamics, a number of unresolved processes need to be modelled in order to produce (realistic) galaxies. These are called 'subgrid' processes. Firstly, radiative cooling and heating of gas is modelled following Wiersma et al. (2009a). This model includes metal line cooling, using the abundances of 9 metal species tracked in EAGLE. It assumes the gas is in ionization equilibrium, including the effect of photo-ionization by a Haardt & Madau (2001) UV/X-ray background.

Secondly, star formation occurs in sufficiently dense ($n_H \gtrsim 10^{-1}\,cm^{-3}$) gas, where the exact threshold depends on the metallicity of the gas (Schaye 2004). The star formation rate of this gas depends on the gas pressure, in such a way that the Kennicutt-Schmidt relation is reproduced by design (Schaye & Dalla Vecchia 2008). Stars, through AGB winds and type Ia and core-collapse supernovae, return metals to their neighbouring gas following Wiersma et al. (2009b). Feedback from star formation is implemented by stochastically injecting thermal energy into a neighbouring SPH particle, heating it by $10^{7.5}$ K. The probability of such a heating event is such that the average energy injected per unit stellar mass matches a set budget (Dalla Vecchia & Schaye 2012).

Finally, in sufficiently massive haloes, a black hole is formed if the halo does not already contain one. The black holes grow by accreting gas and by merging, as described by Rosas-Guevara et al. (2015); Schaye et al. (2015). AGN feedback is implemented by stochastic heating of neighbouring SPH particles, like the supernova feedback, but gas is heated by $10^{8.5}$ K.

The parameters of the feedback processes were calibrated to observations (Crain et al. 2015). Specifically, the simulations were calibrated to reproduce the redshift 0.1 galaxy stellar mass function and stellar-mass-black-hole-mass relation, and to produce reasonable galaxy sizes. The EAGLE galaxy and halo data has been made public by McAlpine et al. (2016), and The EAGLE team (2017) describes the public data release of the full simulation data ('snapshots').

5.2.2 Column density calculations

From this simulation, we calculate column densities by first calculating the ion content of the individual SPH particles (gas resolution elements), then dividing these ions over a dense grid of pixels based on the position and size of each SPH particle.

The ion content of an SPH particle is calculated as

$$M_{ion} = M_g\, Z_{elt}\, f_{ion}, \tag{5.1}$$

where M_{ion} is the total ion mass in the SPH particle. The number of ions in the SPH particle is obtained by dividing this mass by the mass of a single particle of the parent element of the ion. The mass of the SPH particle M_g and the mass fraction in the parent element Z_{elt} (ElementAbundance) are taken directly from the EAGLE output data. The ion fraction f_{ion}, which is the fraction of the parent element nuclei in the desired ionization state, is calculated from the temperature and density of the gas, and the redshift of the EAGLE snapshot. The redshift-dependence comes from the changing UV/X-ray background.

We calculate the ion fractions by linearly interpolating the ion fractions tabulated by Bertone et al. (2010a), as a function of log temperature, log density, and redshift. They calculated the ion fractions using using CLOUDY v7.02 (last documented in Ferland et al. 1998), assuming ionization equilibrium, with photo-ionization by a uniform, redshift-dependent Haardt & Madau (2001) UV/X-ray background. These assumptions are consistent with those made in the EAGLE simulation for the radiative cooling (Wiersma et al. 2009a).

To calculate column densities, we first select a rectangular prism (box) within the EAGLE volume. We choose volumes that span the whole simulated volume in two dimensions ($100 \times 100\,\mathrm{cMpc}^2$), and divide the volume into an integer number of 'slices' along the third axis. This third axis represents the line of sight direction, and for simplicity, we choose it to be parallel to one of the coordinate axes of the simulation (the Z-axis). Note that, relative to simulated structures, this is a random direction. We use different slice depths (numbers of slices), depending on the requirements for the comparison, but our default is 6.25 cMpc. Perpendicular to the line of sight, we divide the box into pixels of $3.125 \times 3.125\,\mathrm{ckpc}^2$.

Given this box and grid, we first select all particles with positions (centres) between the slice boundaries along the line of sight. We assume that their gas mass is distributed according the Wendland (1995) C2 kernel, with its size set by the smoothing length of the SPH particle. We evaluate the kernel at each pixel centre, then normalize the sum of the values to one. Each SPH particle contributes this normalized kernel value times its total ion content to each pixel in the grid. The normalization, and a minimum kernel size (radius) of half the diagonal of a pixel, ensure that mass is conserved in the projection step.

After calculating the number of ions in each rectangular prism in the grid, we simply divide by the area of the pixels to get column densities. The result of this calculation is a map of the column densities in a particular slice of the simulation.

Note that these column densities are an approximation of column densities measured in observations. There, column densities are not measured in a pre-defined spatial grid, but from measured absorption lines, in spectra taken of some background source. The predictions we make are best compared to 'absorption systems': clusters of absorption lines, interpreted as originating from a single object, such as the CGM of a single central galaxy. We have confirmed that the pixels we use are small enough that they match the 'pencil-beam' measurements of column density that would be obtained against a background point source, such as the sources we compare to here (Wijers et al. 2019, Chapter 2). The depth of the slices has some effect on the column density distribution, but this is limited to at most ≈ 0.2 dex at the higher column densities that are potentially observable (Wijers et al. 2019, Chapter 2).

5.3 A blind detection of two O VII absorbers?

5.3.1 The initial detections

Nicastro et al. (2018) used a detailed analysis of X-ray observations of the brightest X-ray blazar, 1ES 1553+113, with *XMM-Newton* to search for soft X-ray absorption along that sightline. The analysis used a total of 1.85 Ms of observations, combining different time periods. This was a blind search, meaning that X-ray absorbers were sought out at any redshift, without any prior expectations. Two absorption systems were found, at redshifts 0.36 and 0.43. They were used to constrain the density of O VII absorbers in the universe. This was also used to estimate the density of the warm/hot 'missing baryons', although the low number of measured data points, and necessary assumptions about e.g., the gas metallicity, make this estimate quite uncertain.

In Fig. 5.1, we show fig. 3 of Nicastro et al. (2018), comparing the number and strength of the absorbers they found to predictions from cosmological, hydrodynamical simulations. Here, we will focus on the comparison of these data to the EAGLE predictions.

The EAGLE predictions for the equivalent width distribution in Fig. 5.1 come from column density distribution predictions. To predict the column density distribution used here,

we used a column density map (§5.2.2) from EAGLE at redshift $z = 0.1$, with a slice depth of 100 cMpc. This redshift does not quite match that of the absorbers, but the difference between redshifts 0.1 and 0.5 in the abundances of O VII absorbers is only ≈ 0.2 dex at column densities of 10^{15}–10^{16} cm^{-2} (Fig. 2.3). The column density distribution is simply a histogram of the column density values in this map. The redshift interval corresponding to this column density map is simply the redshift path covered by each pixel (from the slice depth) times the number of pixels. To convert column densities to equivalent widths, a line width (Doppler parameter) of 100 km s^{-1} was assumed.

The equivalent widths of the measured absorbers are consistent with the EAGLE predictions, although the uncertainties in the measurements are large. This is primarily due to the small number of measured absorbers. Considering the various predictions, this small number is the result of the limited sensitivity (effective area) and spectral resolution of the instruments currently available, making the minimum measurable equivalent width high, and therefore the expected number of detectable absorbers small. This is illustrated by Fig. 2.22; note that an equivalent width of 10 mÅ corresponds to a column density of $\approx 10^{15.5}$–10^{16} cm^{-2}. Note that this nearly 2 Ms observation of the brightest X-ray blazar represents a very optimistic case for a currently feasible blind survey.

In Fig. 2.6 of Chapter 2 (fig. 5 of Wijers et al. 2019), we showed a similar comparison. There, we also give a few more details on the predictions of Cen & Ostriker (2006) and Branchini et al. (2009). There are, however, a few differences between the two figures.

Firstly, the data points from in Fig. 5.1, taken from Nicastro et al. (2018), are different from the measurements shown in Fig. 2.6. This is because the Fig. 2.6 data points include a revision of one of the measured equivalent widths by Nicastro (2018). This revision was based on revised atomic data for the N II Kα triplet, meaning a Galactic absorption line would be blended with the higher-redshift ($z = 0.4339$), higher-equivalent-width absorber of Nicastro et al. (2018). The absorber was still detected, but at lower significance (2.9–3.3σ instead of 4.1–4.7σ for the single line) and with a lower equivalent width (10 ± 3 mÅ instead of 14.7 ± 3.1 mÅ). These revised data points are consistent with all the simulation predictions shown in Fig. 5.1.

Secondly, we refined the EAGLE prediction for Fig. 2.6 (Chapter 2, Wijers et al. 2019). We still use column density distributions from column density maps as a starting point. However, we use two different distributions in Fig. 2.6, and compare the results: we start from maps with a 100 cMpc slice depth, as shown in Fig. 5.1, and from maps with 6.25 cMpc slice depths, dividing the simulation volume into 16 slices. Fig. 2.6 shows that this makes relatively little difference at the scale of the figure.

We also refined the way in which we convert column densities to equivalent widths. Instead of assuming a line width, we used a distribution of equivalent widths in bins of column density, calculated from synthetic spectra through the EAGLE volume (for more details, see Chapter 2, Wijers et al. 2019). The column densities and equivalent widths were summed over the full 100 cMpc sightlines we calculated the spectra for. Further improvements, resulting in the column-density-equivalent-width relations in Fig. 3.7 (Chapter 3, Wijers et al. 2020) were not included in Fig. 2.6.

In Fig. 2.21, we showed that scatter in the relation used to convert the column density distribution to an equivalent width distribution has relatively little impact on the resulting equivalent width distribution in the range shown in Fig. 5.1, relevant to this comparison. The line width (Doppler parameter) of 90 km s^{-1}, derived from the virtual spectra and used in that comparison, is similar to the value of 100 km s^{-1} used in Fig. 5.1, and the maximum effect of this difference is a small: a 10 per cent horizontal shift of the curve. All in all, the

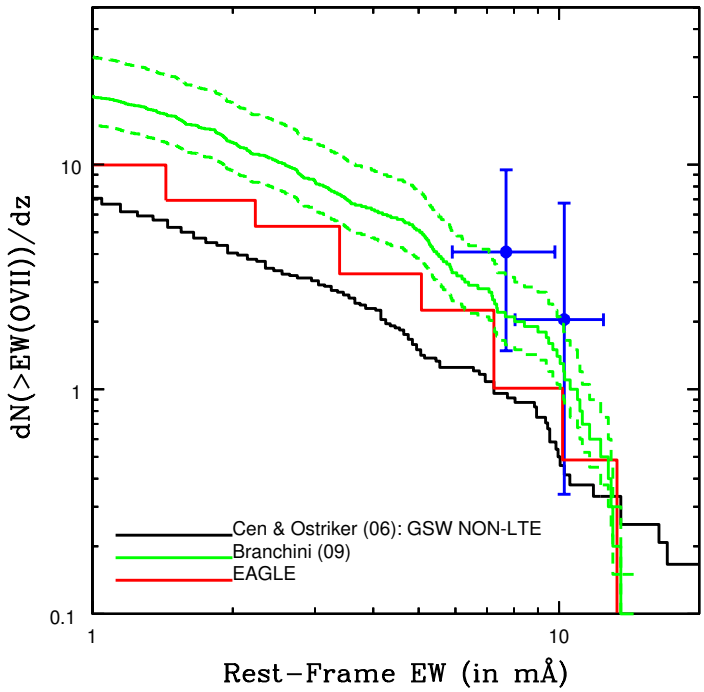

Figure 5.1: Comparison of the O VII (He-α recombination line) rest-frame equivalent width distribution measured by Nicastro et al. (2018) to predictions from cosmological, hydrodynamical simulations; the figure is fig. 3 from Nicastro et al. (2018). The curves and data points show the cumulative number of absorbers (i.e., the number above the equivalent width on the x-axis) per unit redshift. The blue data points show the equivalent widths of the two Nicastro et al. (2018) absorbers. The black curve shows the prediction of Cen & Ostriker (2006), using their model with galactic stellar winds, and with O VII to total oxygen ratios calculated without assuming ionization equilibrium. The green lines show the predictions of Branchini et al. (2009). The red line shows the predictions from EAGLE (Schaye et al. 2015), calculated from the 100^3 cMpc^3 reference EAGLE volume at redshift 0.1. For EAGLE, column densities were calculated along 100 cMpc sightlines, and converted to equivalent widths assuming a fixed line width (Doppler parameter) of 100 km s^{-1}.

effects of these refinements are small.

Third, the selection of data from Branchini et al. (2009) and Cen & Ostriker (2006) is different. Fig. 5.1 shows an additional Cen & Ostriker (2006) model, where ionization fractions were computed assuming ionization equilibrium. In contrast, we only show one of the Branchini et al. (2009) models. This model uses their more realistic model for the gas metallicity (including scatter in the metallicity-density relation they use), which also predicts the highest absorber densities of their models in the equivalent width range shown.

All in all, with or without these refinements to the measurements and predictions, the EAGLE predictions agree with the absorber densities measured here. The large uncertainties in the measurements mean that this is mostly a sanity check, however, as the measurements are consistent with the predictions of the other simulations as well.

5.3.2 A further investigation of the absorber environments

Johnson et al. (2019) investigated these absorbers further, using a follow-up galaxy redshift survey along the line of sight to the blazar. One absorber ($z = 0.4339$) is suspected to come from the IGrM of the blazar host group. This is based on a determination of the blazar redshift, from the redshifts of Lyman-α absorbers in its spectrum (the Lyman-α forest), and a distribution of redshift differences between quasars and their highest-redshift Lyman-α absorbers. This redshift is consistent with a galaxy group found in the redshift survey (light-weighted $z = 0.433$), indicating that this group is most likely the blazar host. The group is also the only group found along the sightline, and a galaxy group is the expected environment for a blazar like 1ES 1553+113. The redshift of this group and the blazar match that of the high-redshift absorber of Nicastro et al. (2018), which therefore most likely is IGrM absorption from the blazar host. Non-detections of O VIII or O VI absorption at the same redshift indicate that the gas is collisionally ionized rather than photo-ionized, meaning absorption must come from relatively dense gas. This supports the idea that the absorber is part of the IGrM, not nearby WHIM.

Nicastro et al. (2018) did not identify this group because they used used photometric galaxy redshifts in their analysis, with much larger redshift errors. They did argue the O VII absorption was not intrinsic to blazar outflows, based on its lack of time variability, or to the blazar host galaxy ISM, based on the lack of UV absorber counterparts.

The absorber intrinsic to the blazar host group cannot be used for a determination of the column density distribution of O VII and estimates of the hot gas of the universe overall, at least without additional assumptions. This is because it is not a *random* absorber along the line of sight, as it is connected to the blazar used as a backlight.

The estimated blazar host group dynamical mass is $2\text{–}5 \times 10^{13}\,\mathrm{M}_\odot$; at those masses, an O VII absorber of $10^{15.8}\,\mathrm{cm}^{-2}$ (Nicastro 2018) is consistent with EAGLE expectations, shown as the yellow and orange lines in Fig. 3.8. Note that we expect about half the column density in the group to lie behind the blazar. In EAGLE, such an absorber is more likely in groups at the lower end of the estimated mass range, assuming the dynamical mass is similar to M_{200c}.

The EAGLE analysis of Johnson et al. (2019) focussed on the second absorber, at $z = 0.355$. The galaxy redshift survey yielded no galaxies within 630 pkpc of the absorber, and within $1000\,\mathrm{km\,s}^{-1}$. We predicted how rare or common it would be for an absorber as strong as the measured one ($10^{15.6}\,\mathrm{cm}^{-2}$; Nicastro et al. 2018) to be found so far from any galaxies. This is generally unexpected, as the detected oxygen must have been produced in a galaxy.

In order to do this, we used *conditional* column density distributions. We used the catalogues of McAlpine et al. (2016), listing galaxy positions and stellar masses in EAGLE to create 'masks' for the EAGLE column density maps. A mask is a selection of pixels in the column density maps meeting particular criteria. In this case, we selected pixels at a minimum distance (630 pkpc) from any galaxy above a given stellar mass ($10^{9.7}\,\mathrm{M}_\odot$). These are the impact parameter and stellar mass for the closest galaxy Johnson et al. (2019) found to the $z = 0.355$ absorber. We then created a column density distribution using only these pixels, and compared it to the distribution for all pixels. The ratio of the two gives the probability that an absorber of a given strength is found to be as isolated as the one claimed by Nicastro et al. (2018), once galaxy information is included.

We also tested the probability for distances > 2273 pkpc from $\mathrm{M}_\star > 10^{11.2}\,\mathrm{M}_\odot$ galaxies, based on a more distant galaxy with a larger halo virial radius, but we found the distance to the less massive galaxy to give stronger constraints. Both galaxies are estimated to lie about five virial radii from the absorber.

We used column density maps with a slice thickness of 33.3 cMpc (3 slices), at a redshift

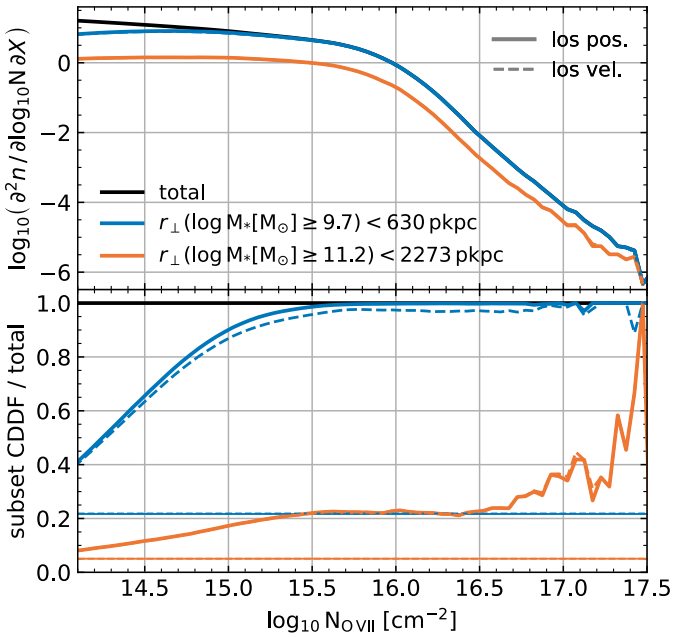

Figure 5.2: The EAGLE O VII column density distribution function (CDDF) at $z = 0.37$, measured from column density maps with a slice thickness of 33.3 cMpc, corresponding to a Hubble flow velocity of $\approx 2000\,\mathrm{km\,s^{-1}}$. The top panel shows the absorber incidence rate, with respect to the absorption length dX (eq. 2.2). In the top panel, the black line shows the total column density distribution, while the coloured lines show the density of absorbers that are *not* as isolated as the $z = 0.36$ absorber of Nicastro et al. (2018). We measure the level of isolation using a minimum distance to any galaxy above a given stellar mass. Based on two galaxies Johnson et al. (2019) found in the vicinity of the absorber, we use a minimum distance (impact parameter) of 630 (2273) pkpc from any galaxy with a stellar mass greater than $10^{9.7}$ ($10^{11.2}$) $\mathrm{M}_\odot$. Along the line of sight, we only consider galaxies that lie in the same slice as each absorber for these distance determinations ('pos.'; solid curves). However, in reality, only the redshifts of the absorbers and galaxies are known. These depend on their peculiar velocities as well as their positions along the line of sight. Therefore, we also select galaxies in the same slice in a different way to produce the dashed curves ('vel'). First, we adjust the galaxy line of sight positions according to their peculiar velocities. Then, we determine the distances (impact parameters) between absorbers and galaxies that lie in the same slice according to their modified positions. Note that we do not account for the peculiar velocities of the absorbers. The bottom panel shows the fraction of the total number of absorbers at each column density contributed by each absorber category. Thin, horizontal lines show the fraction of the sky meeting each of the non-isolation criteria. In EAGLE, O VII absorbers as strong as the $z = 0.355$ system claimed by Nicastro et al. (2018) are rarely as isolated as it is found to be by Johnson et al. (2019).

of 0.37, close to that of the absorber. The slice thickness was chosen to match the velocity range over which Johnson et al. (2019) searched for galaxy neighbours to the absorbers; the Hubble flow over 33.3 cMpc at $z = 0.37$ is $\approx 2000\,\mathrm{km\,s^{-1}}$.

To match the galaxies to these absorbers, we primarily consider the (impact parameter) distances to galaxies that lie (spatially) between the boundaries of each simulation slice along the line of sight. Our column density maps divide the simulation only spatially, without considering the peculiar velocities of the absorbing gas.

To roughly estimate the impact of peculiar velocities, we also consider distances to galaxies selected for each slice in a different way. Here, we adjust the galaxy positions (in physical coordinates) along the line of sight by the ratio of the galaxy peculiar velocity to the Hubble constant $v_{pec} / H(z)$. We then determine whether a galaxy should be cross-matched with a particular slice by comparing the slice edges to these adjusted galaxy line of sight positions. Note that this is a conservative estimate of how bad the effect of ignoring peculiar velocities is, since they are not considered for the gas in the column density maps, which means there is a mismatch between the gas and galaxy redshifts here that would not be present in the observations, aside from errors.

We find that the probability that an absorber with an O VII column density $\geq 10^{15.6}\,\mathrm{cm^{-2}}$ would be located ≥ 630 pkpc from any galaxy within $\pm 1000\,\mathrm{km\,s^{-1}}$ and with $M_\star \geq 10^{9.7}\,M_\odot$ is 1 per cent using the position-based galaxy-absorber matching. Using the velocity-shifted galaxy matching, the probability is 3 per cent, with the difference most likely the result of galaxies being velocity-shifted away from their associated absorbers. The number density of such isolated, high-column-density absorbers in EAGLE $\mathrm{d}n(> 10^{15.6}\,\mathrm{cm^{-2}}, \mathrm{iso.}) / \mathrm{d}z$ is 0.17, using the position-based galaxy matching. This means that over the $\Delta z \lesssim 0.43$ redshift path probed along this sightline, the absolute probability of detecting such an absorber is low ($\lesssim 0.07$), according to EAGLE.

For comparison, Bonamente (2019) estimated the chance that a noise fluctuation of at least the size corresponding to the measured absorber would arise somewhere along a redshift path of this length is 4 per cent. This is for a single line, excluding the higher-redshift line from the re-analysis on the grounds that it is not a 'random' absorber.

Therefore, the second absorber may be real, albeit detected at low significance, which would be in tension with EAGLE predictions because of its isolated nature. This may be due to low-mass (in EAGLE, unresolved, and in the survey, undetectable) galaxies producing metals, and possibly hot gas in outflows, that are absent in EAGLE. Alternatively, outflows from the detected galaxies may reach larger distances from the galaxies than predicted by EAGLE, or the temperature of the metal-enriched outflows may be underestimated in EAGLE.

On the other hand, the spectral feature identified as the second absorber may in fact just be noise. The absence of such an absorber would be consistent with EAGLE predictions. Note that Johnson et al. (2019) also analyse the distances to galaxies of broad H I, O VI, and narrow H I absorbers, and conclude that metals likely do not typically reach the distances from galaxies where the $z = 0.355$ O VII absorber of Nicastro et al. (2018) was found.

5.4 Soft X-ray counterparts to FUV absorbers

Next, we consider absorbers that were found using targeted searches. The goal of Ahoranta et al. (2020) and Ahoranta et al. (2021) was to detect X-ray absorption by searching at the redshifts of known FUV absorbers (H I and O VI). They started from a sample of 16 sightlines with UV and X-ray spectra with sufficiently high signal-to-noise ratios for their analysis (J. Ahoranta, priv. comm.). In the UV spectra, there were 11 O VI absorbers, and 12 broad H I

absorbers (Doppler b parameters $> 70\,\mathrm{km\,s^{-1}}$). The line width criterion for H I was used to select warm gas; though the broadening may not be thermal, an absorber with a narrow line is definitely not warm. They searched for a variety of X-ray absorption lines at the redshifts of these absorbers, including O VII, O VIII, Ne IX, and Ne X.

They investigated all 23 redshifts, and found X-ray counterparts to two of the O VI absorbers. The number of absorbers studied here is therefore small, and the selection effects are strong, as current X-ray instruments are only sensitive to the strongest absorption lines. No counterparts to broad H I absorbers were found. Because we only have two detected counterparts, we do not know whether this is a coincidence, or a result of different X-ray counterpart populations to broad H I and O VI. Therefore, it is uncertain whether the strength of the selection effect should be calculated relative to the number of O VI redshifts investigated or the total number of redshifts. However, given the uncertainties that come with the small numbers of detected absorbers, this difference is relatively small. We estimate that the detected absorbers represent the ≈ 10–20 per cent strongest counterparts to O VI absorbers in the population.

In these works, the absorption systems have measured column densities for at least two ions (O VI and the X-ray absorber), and upper limits on others. Because the O VI redshifts were used as priors in the X-ray absorber search, we are not looking at random X-ray absorbers. We include this selection effect in the comparison to EAGLE by examining the properties of absorption systems with O VI column densities that match the measured values. We note that 'counterparts' in EAGLE may have arbitrarily low column densities, including zero, so the EAGLE predictions properly account for both undetectable and absent X-ray counterparts.

Our starting point for these comparisons is a set of EAGLE column density maps for each ion that was measured or constrained observationally. Here, an absorption system is defined by a pixel in a column density map of a given 'slice' of the simulation volume (see §5.2.2). We 'match' column densities for the different ions simply by comparing column densities in matching pixels. For these works, we used slices with a depth of 6.25 cMpc, and a simulation 'snapshot' at redshift $z = 0.1$.

The redshift is close to the redshifts of the X-ray absorbers that were found, as well that of an O VI absorber in the 3C 273 spectrum for which no X-ray counterpart was found. The path length for the initial 16 sightlines was $\Delta z \approx 2$, and for the nine sightlines where the UV absorbers were found, $\Delta z \approx 1$, so the redshift $z = 0.1$ EAGLE snapshot is reasonably representative of the redshifts searched.

The slice depth corresponds to a Hubble flow velocity $\Delta v = 404\,\mathrm{km\,s^{-1}}$, though we note that our slicing only accounts for the positions of SPH particles along the line of sight, and not their peculiar velocities. Peculiar velocities can be similar to the Hubble flow over this slice depth, so this velocity range does not necessarily correspond to the velocity range an absorption system would have.

We also compare temperatures for the different absorbers. For this, we make maps of ion-weighted temperatures (for the different ions), alongside the column density maps. For these maps, we take the temperature of each SPH particle contributing ions to a given pixel, and weight the temperatures by each particle's ion contribution. We compare temperatures for each gas phase to the ion-weighted temperature for a representative ion for that phase.

5.4.1 System 1: 3C 273, redshift 0.09

The first absorption system that we will discuss is from Ahoranta et al. (2020). They searched for X-ray absorption lines in the spectrum of quasar 3C 273, at the redshifts of two O VI absorbers from Tilton et al. (2012), and found an X-ray counterpart to one of them. They found O VIII and Ne IX absorption lines at redshift $z = 0.09$. For O VII, an upper limit was obtained. Its He-α line would be blended with a Galactic O I line at this redshift, meaning the constraints come from weaker O VII lines like He-β.

These lines were found by combining archival measurements taken at different times, with different instruments: the *XMM-Newton* RGS and *Chandra* LETG (ACIS and HRC) and HETG (MEG), for a total of ~ 1 Ms of data. To avoid artefacts, they stacked spectra from the same instrument (but taken in different observations), and fitted the stacked data from different instruments jointly. In these fits, the continuum (fitted with a spline function) was allowed to vary between the stacked spectra for the different instruments, but the absorption model (Galactic and extragalactic) was not. This is reasonable because the observations were taken at different times and 3C 273 is a variable source. The data analysis was done carefully, to avoid issues like artefacts in the stacked spectra that could be confused with absorption lines.

The data were fit with two different models for the extragalactic absorption system: a 'slab' model and a 'CIE' model. The CIE (collisional ionisation equilibrium) model assumes the X-ray absorption comes from one gas cloud in collisional ionization equilibrium, with solar relative abundances. Note that the metallicity is degenerate with the hydrogen column in these fits, since only metal lines are measured (outside our Galaxy). The slab model fits the absorption lines from the different transitions of each ion, to measure each ion's column density independently. Because the absorption line shapes are unresolved, a line width (Doppler b parameter) $b = 100\,\mathrm{km\,s^{-1}}$ was assumed in these fits. In our comparisons, we generally use the slab model constraints on the column densities of each ion, and the CIE model for the temperature of the absorption system.

The slab model yielded a 3.9σ joint detection of O VIII and Ne IX, which trace gas at similar temperatures in CIE, and are thus assumed to represent a single gas phase. The assumption of collisional ionization is motivated by our predictions in Chapter 2 (Wijers et al. 2019), where we predict that the high column density absorbers detectable with current instruments should be collisionally ionized. This model adequately fits the data. Its temperature is constrained from above by the non-detection of Fe XVII absorption, and from below by non-detections of O VII and N VII.

The X-ray CIE model predicts an O VI column density of $10^{12.2\pm0.2}\,\mathrm{cm^{-2}}$, well below the $10^{13.26}\,\mathrm{cm^{-2}}$ column density measured in the FUV spectrum (Tilton et al. 2012). The observed O VI lines are also narrower than predicted by thermal broadening at the best-fit CIE temperature for the X-ray lines. This is evidence that the measured X-ray absorbers are tracing hot gas, and the O VI measured in the FUV spectrum is tracing a different, warm gas phase.

In Fig. 5.3, we compare the O VIII and Ne IX column densities measured in the X-ray spectra to the predicted values for counterparts to an O VI absorber with the same column density as the $z = 0.09$ system (right panel). The X-ray ion column densities are higher than is typical in EAGLE. However, they seem consistent with the strongest $\approx$ 10–20 per cent of predicted X-ray counterparts, which is the X-ray absorber selection effect we estimated from UV counterpart non-detections. The measured values are consistent with EAGLE expectations at the 1–2σ level.

In the right panel of Fig. 5.3, we modify the absorption system sample by adding a selec-

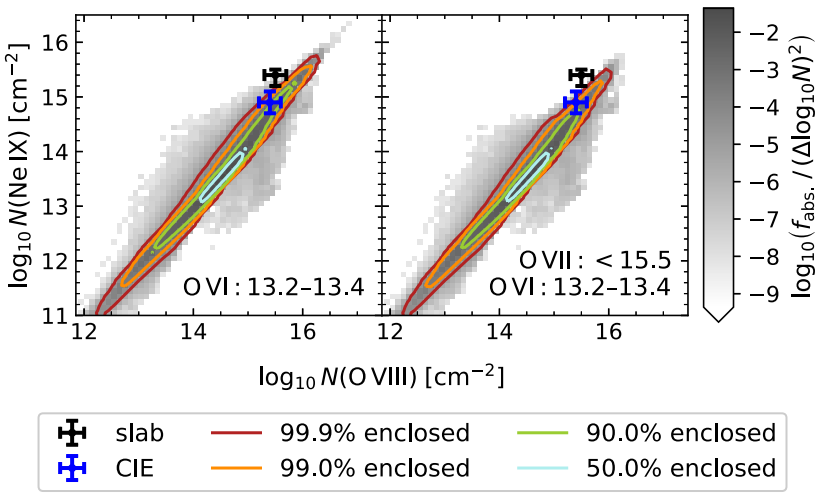

Figure 5.3: The measured O VIII and Ne IX column densities at $z = 0.09$, compared to EAGLE predictions for counterparts to the $z = 0.09$ O VI absorber. This is fig. 9 from Ahoranta et al. (2020). The measured column densities are indicated in blue and black, with 1σ error bars. The 'slab' column densities were measured for each ion individually, by fitting gaussian absorption lines for each transition of the ion. The 'CIE' column densities were instead fit to the X-ray data assuming the O VIII and N IX absorption arises from the same gas, in collisional ionization equilibirum (CIE) and with solar metal abundance ratios. For the EAGLE predictions, we show a histogram of individual absorption systems and contours enclosing the fractions of absorption systems indicated in the legend. We only show absorption systems with ion column densities ($\log_{10}$ cm^{-2}) in the ranges indicated in the bottom right of each panel. These constraints match the measured O VI column density (1σ range) and the 'slab' model upper limit on the O VII column density, considering the $\approx$ 80–90 per cent of O VI (UV) absorbers for which no X-ray counterpart was found.

tion criterion: the O VII column density must agree with the measured constraint. We find this has fairly little effect on the predicted O VIII and Ne IX column densities.

In Fig. 5.4, we compare the EAGLE predictions to the measured temperature of the absorber. A single CIE model was found to be inconsistent with the combined UV and X-ray data, so the FUV O VI absorber is assumed to represent a different, warm phase. The temperature of this phase is most strongly constrained by the X-ray data. With the O VI column density fixed to the best-fit value from the FUV data, X-ray upper limits on the O IV, O V, and O VII column densities constrain the temperature of the absorber.

In Fig. 5.4, we plot the warm and hot phase temperatures predicted by EAGLE, measured as the O VI and O VIII-weighted temperatures, respectively. We plot these temperatures for absorption systems meeting the various column density constraints listed in the panels. The O VI constraint is the 1σ range of Tilton et al. (2012), the other constraints are the upper limit and 1σ ranges from the slab model X-ray measurements.

When all the measured column densities are considered, the EAGLE predictions agree well with the measured temperatures. EAGLE also clearly predicts that, at these column densities, the gas should consist of two different phases. Without the O VII upper limit, a single-phase solution is still allowed; the constraint on this 'intermediate' ion is needed to exclude such a single-phase solution in EAGLE. The strongest single constraint is provided

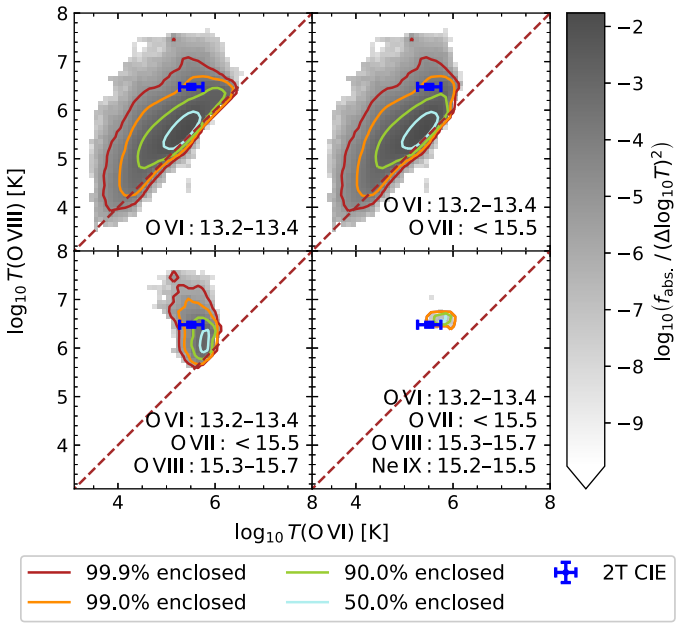

Figure 5.4: A comparison of the hot and warm phase temperatures predicted from EAGLE to those measured using a two-component CIE fit to the measured X-ray and UV data towards the quasar 3C 273 at $z = 0.09$; this is fig. 10 from Ahoranta et al. (2020). The measurement is indicated in blue, with 1σ error bars. For the warm and hot phase temperatures in EAGLE, we use the O VI and O VIII-weighted temperatures, respectively. The grey histogram and coloured contours indicate the distribution of ion-weighted temperatures found in EAGLE. The contours show different enclosed fractions of EAGLE absorption systems, as indicated in the legend. We only show absorbers with ion column densities ($\log_{10}$ cm^{-2}) in the ranges indicated in the bottom right of each panel. These constraints match the measured column densities and upper limits of Tilton et al. (2012) (O VI) and Ahoranta et al. (2020) (other ions). Specifically, we use the column densities and upper limits that Ahoranta et al. (2020) obtained using a 'slab' model, where the column densities of each ion are measured individually, by fitting gaussian line models to each ion's absorption line(s) independently.

by Ne IX. Considering the relative frequency of absorbers of these four ions at their measured column densities, the Ne IX absorber is also the rarest in EAGLE (Fig. 3.5).

All in all, the $z = 0.09$ X-ray absorber in the 3C 273 quasar spectrum seems to match the EAGLE predictions, considering the observational selection effects on the strength of the X-ray absorption lines. The agreement between the temperatures, given the absorption system column densities, will largely be a consequence of the CIE conditions in high-column-density absorbers, which means they will not be a very sensitive test of the EAGLE model. The comparison between the counterpart column densties is more sensitive, although we note that the correlation between the O VIII and Ne IX column densities will largely be driven by the similar gas in which these ions arise (Fig. 3.1).

Additional analysis of galaxy distributions from SDSS around the sightline to quasar 3C 273 revealed two filaments crossing the sightline around the redshift of the absorption system. Given the uncertainties, both filaments are consistent with the redshift of the X-ray absorbers, but only one is consistent with the O VI redshift. There is also a Milky-Way-like galaxy within the filament at a redshift consistent with the absorption system, at an impact

parameter of 500 kpc.

As the origin of the absorption system, this is consistent with the (large) range of column densities predicted from such a galaxy and impact paramater in the IllustrisTNG simulation (D. Nelson, priv. comm. with Ahoranta et al. 2020). This also seems consistent with EAGLE predictions for O VI (Fig. 3.10). The O VIII and Ne IX column densities are relatively high for those stellar masses and distances, though the O VII upper limit is consistent with expectations. In EAGLE, absorbers with the measured O VIII column density could come from the CGM or filament gas (Fig. 3.6). The O VII upper limit is similarly consistent with both interpretations, but the Ne IX column density would most likely come from the CGM in EAGLE, albeit that of haloes somewhat more massive than that hosting the Milky Way.

5.4.2 System 2: Ton S 180, redshift 0.046

Ahoranta et al. (2021) found the second absorption system we discuss here in the spectrum of the Seyfert galaxy Ton S 180, at $z = 0.046$. For the UV analysis, data from *FUSE* (Far-Ultraviolet Spectroscopic Explorer) and *STIS* (Space Telescope Imaging Spectrograph) on the Hubble Space Telescope were used. The spectra were stacked for analysis, but were also separately fit with a joint model in the same way as the X-ray spectra of §5.4.1 (Ahoranta et al. 2020) to verify the results.

The starting point for this analysis was a known feature in the Ton S 180 spectrum, at $z = 0.0456$ (e.g., Danforth et al. 2006; Tilton et al. 2012). Ahoranta et al. (2021) analysed the FUV spectra and found an O VI absorber at this redshift, with another O VI absorption component, H I (Lyman α and β), and C III nearby.

This redshift was the starting point in the search for an X-ray absorber in the Ton S 180 spectrum. For this system, 200 ks of data were available for both RGS instruments on *XMM-Newton*. Some *Chandra* data were also available, but the exposure time was too short, meaning the constraining power of those observations would be very poor. Therefore, only *XMM-Newton* data were used in this analysis. Like in §5.4.1, the spectra from the different instruments and observing times were processed separately, and fitted jointly. The absorption components were fixed between the models for the different spectra, but the intrinsic spectrum of Ton S 180 was allowed to vary. The X-ray spectra were fitted in the same way as in §5.4.1, using slab models to measure individual column densities from each ion's transitions, and a CIE model to fit the temperature of the gas.

Using the slab model, Ahoranta et al. (2021) found an O VII absorber at 5σ significance. An O VIII absorber is not detected in a statistically significant way, but Ahoranta et al. (2021) did fit its column density. As can be expected, the uncertainties on this column density are large.

In Fig. 5.5, we compare the measured O VII column density to what would be expected from EAGLE, given the column density and temperature of the O VI absorption system. The distribution of EAGLE O VI and O VII column densities is shown in the histogram, while the lines show percentiles of the O VII column density distribution at fixed O VI column density. For these distributions, we split the sample by O VI-weighted temperature, at the 3σ upper limit on the temperature of the FUV absorption system. This limit was calculated from the upper limit on the width of the O VI line in the FUV spectrum, assuming pure thermal broadening.

The measured O VI column density from the FUV spectrum is shown with the vertical band. The red cross shows the measured column density of O VII, and O VI column density inferred from the FUV spectra and the CIE model fit to the X-ray data. The column density

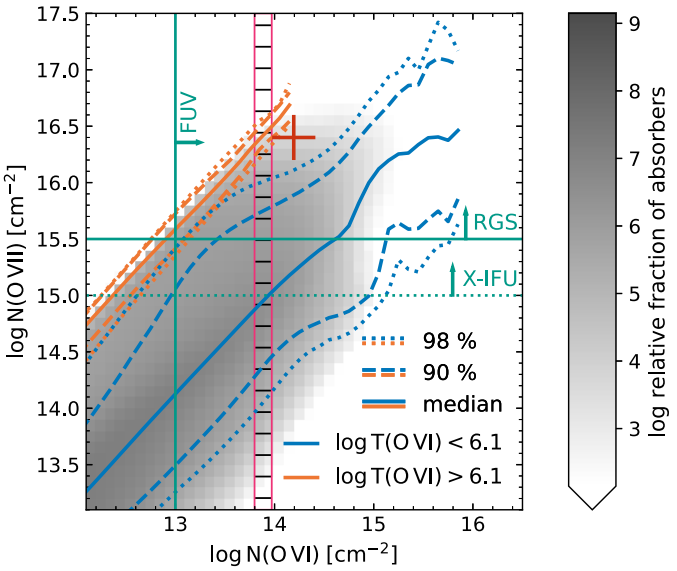

Figure 5.5: The predicted correlation between O VI and O VII column densities from EAGLE. This is fig. 8 from Ahoranta et al. (2021). The column densities are from the $z = 0.1$ EAGLE snapshot, using a slice depth of 6.25 cMpc. The histogram (grey) shows the distribution of all absorbers. The lines show median O VII column densties, and enclosed fractions of O VII absorption systems, at fixed O VI column density. The lines show these percentiles for O VI absorption systems with O VI-weighted temperatures as indicated in the legend; the limit corresponds to the measured 3σ upper limit on this temperature. The lines show estimated detection limits for different instruments. The O VI limit is for *HST-COS*, and the O VII limits are for the *XMM-Newton* RGS, and the future Athena X-IFU. The vertical band (horizontally dashed) shows the measured O VI column density from the FUV spectrum (1σ range), and the red cross shows the measured O VII column density and the total O VI column density, inferred from the FUV spectrum and ionization modelling of the X-ray data, with 1σ error bars.

of O VII was measured using the CIE model at the best-fit redshift of the X-ray absorption system. For the O VI column density, we add the two FUV component column densities from the vertical band to the O VI column density inferred from the CIE model.

At first glance, the large O VI column density in gas at $1.7 \pm 0.2 \times 10^6$ K, inferred from the CIE model X-ray fit, is inconsistent with the measured upper limit of 1.4×10^6 K for the O VI column density in the FUV spectrum. Ahoranta et al. (2021) found that these FUV and X-ray O VI predictions can nonetheless be reconciled. From the X-ray data, no O VI transitions can be measured; the column density for this ion is merely inferred. In the FUV data, a very broad O VI absorber, as predicted by the CIE model, is undetectable, due in part to degeneracies with the continuum model, even with the inferred column density of $10^{13.9\pm0.2}$ cm^{-2}.

In EAGLE, absorption systems with at least the O VI column density measured from the FUV data, and with a temperature below the measured 3σ upper limit, usually have lower O VII column densities than the one measured here. This is true even considering that only the strongest $\approx$ 10–20 per cent of X-ray counterparts were found. However, the O VI inferred to be present in this absorption system includes a hot component as well as the FUV-measured warm phase. In the EAGLE predictions, those phases would both contribute to the ion-weighted temperature. Therefore, the observed system could end up with a temperature

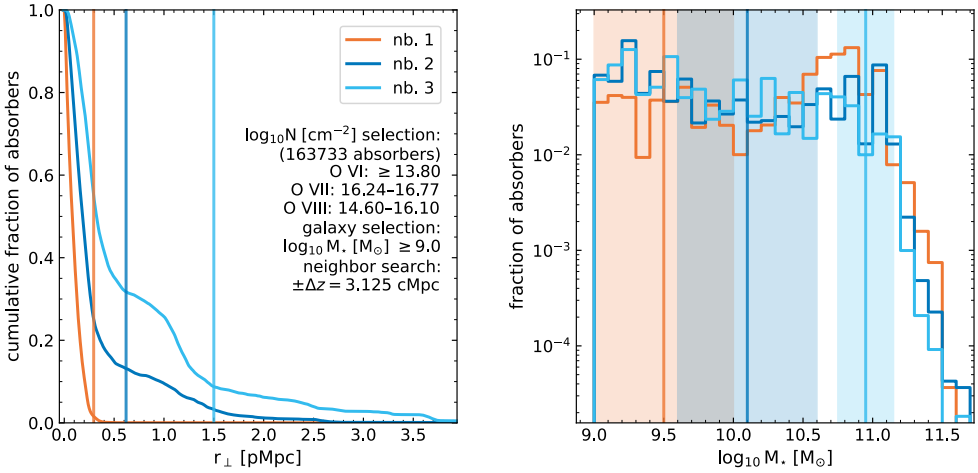

Figure 5.6: A comparison of the galaxy environment of the measured absorption system to predictions from EAGLE. The left panel is fig. 9 from Ahoranta et al. (2021). We search for the nearest neighbour galaxies in the same slice of the EAGLE simulation as absorbers with column densities like the measured ones. For the O VII and O VIII column densities, we use the 1σ ranges of slab column densities, measured at the redshift of the O VI absorber. For O VI, we require a column density at least as large as the best-fit (total) column density measured in the FUV spectrum. We also allow higher column densities because the CIE model predicts a broad O VI absorber in the same gas phase as the X-ray lines, with similar column density to the FUV system. We search for galaxies with stellar masses $M_\star \geq 10^9\,M_\odot$, which is roughly the detection limit in the survey. The left panel shows the distances (impact parameters) of these galaxies to the absorbers. Vertical lines show the measurements, the curves show the cumulative distributions from EAGLE. The neighbours are numbered from closest (nb. 1) to third closest (nb. 3). The measured absorber is relatively far from galaxies compared to EAGLE, and especially far from the closest galaxy. The right panel shows the distribution of stellar masses, as the fraction of absorbers per neighbour stellar mass bin ($\Delta \log_{10} M_\star = 0.1$). The measured masses and 1σ errors are shown by the vertical lines and bands. This seems consistent between EAGLE and the measured system, but as the neighbour stellar mass distribution is quite flat, this is not a very informative comparison.

above the warm-phase upper limit in the EAGLE data, depending on the actual temperature of the warm phase. The measurements are consistent with an O VI temperature determined by the hot phase rather than the warm phase.

Due to these complications, it is difficult to account for the prior information on the temperature of FUV O VI absorber in the EAGLE analysis. Because the majority of the O VI systems in EAGLE are below the temperature limit, ignoring temperature constraints would yield predictions very similar to those for $T < 10^{6.1}$ K O VI absorption systems. Therefore, the column density of the O VII absorber is higher than than expected from the column density of the FUV O VI absorber, even considering the non-detections of X-ray counterparts to $\approx$ 10–20 per cent of the O VI (UV) absorbers. However, given the temperatures inferred for the two phases, the combination of inferred total O VI and O VII column densities is plausible.

We note that the O VII slab model column densities, inferred from only the O VII transitions, are higher than the CIE model values, but the 1σ lower limits are similar. The level of (in)consistency between the measured data and EAGLE therefore does not depend too strongly on how the O VII column density is measured.

To investigate the source of the absorption, Ahoranta et al. (2021) searched for galaxies in

a 9×9 pMpc region around the absorber on the sky, with a depth of 4 pMpc. They estimated the stellar masses of the galaxies based on their B, R, and K-band photometry, and their halo masses from a stellar-mass-halo-mass relation. The absorber was found to be outside their virial radii, though the closest three are within ≈ 2–$3\,R_{200c}$.

We compare the distances and masses of these galaxies to those of the closest neighbour galaxies to EAGLE absorbers with column densities similar to those measured in the Ton S 180 sightline. We match galaxies to absorbers by considering galaxies with the centres of mass within the same slice as the absorber. We do not include any peculiar velocity adjustments like those in §5.3.2. We used 6.25 cMpc slices, which is smaller than the line of sight search region used in the observations. However, the observed galaxies are the closest even in a wider range of relative velocities (Ahoranta et al. 2021, fig. 9). Additionally, including galaxies up to 3.125 cMpc from the slice edges ($\pm\Delta z = 6.25$ cMpc) in the neighbour search makes little difference for the level of agreement between EAGLE and the observations. This means the larger search region in EAGLE should not matter very much for the comparison.

When comparing EAGLE O VI column densities to the observations, we consider the column density measured in the FUV spectrum to be a lower limit. This is because the CIE model fitted to the X-ray data predicts an O VI absorber produced by the same warm-hot gas producing the X-ray lines, with a column density similar to that of the FUV absorber. We note that the EAGLE column densities measure all O VI, and are insensitive to the shapes of any absorption lines. For O VII and O VIII, we use the slab model column densities, measured at the redshift of the FUV O VI absorber, with their 1σ error ranges. We only consider EAGLE galaxies with stellar masses $\geq 10^9\,M_\odot$ in the neighbour search, matching the estimated limit of the survey used in the observations.

We find the nearest neighbours in EAGLE, and compare the distances (impact parameters) between these neighbours and the absorber, and the neighbour's stellar masses, to the measured values in Fig. 5.6. EAGLE predicts absorbers closer to galaxies than found here, though only the nearest neighbour distance represents a clear tension. The neighbour stellar mass distributions are fairly flat up to $\approx 10^{11}\,M_\odot$, so 'extreme' values in the distribution are not really less likely than more 'central' values, and we plot the differential distribution rather than the cumulative distribution. The stellar masses of the neighbours are consistent with the measured values. However, the broad distribution of neighbour stellar masses in EAGLE, combined with the single absorber we compare to, mean that this comparison is mostly a sanity check.

Ahoranta et al. (2021) also made rough estimates of the metallicity of the hot gas, using upper limits on the H I column density associated with this phase. The Lyman α line arising from the hot phase would be blended with two nearby Lyman α lines, and parameters such as the line width are uncertain, so these are somewhat rough estimates.

The estimated 3σ (5σ) lower limit on the metallicity is $0.8\,Z_\odot$ ($0.5\,Z_\odot$). This would be higher than expected for typical IGM gas (e.g., Martizzi et al. 2019), though consistent with O VI–VIII-weighted metallicities up to at least $\sim 3\,R_{200c}$ from galaxies with a wide range of halo masses (e.g., Chapter 3, Wijers et al. 2020). The high metallicity may therefore indicate a particular connection to a nearby galaxy, such as a far-reaching outflow, but it may also be a common value for absorbers discovered through metal line absorption.

In short, like the previous absorption system, this one has higher X-ray column densities than would be expected based on the column density of the O VI absorber. Unlike for the 3C 273 absorber, this seems true even considering that $\approx$ 80–90 per cent of O VI (UV) absorbers had no observed counterparts. However, given 11 (23) independent trials, there is a probability of $1 - 0.99^{11} = 0.1$ (0.2) of finding at least one absorber stronger than the

99^{th} percentile of the X-ray column density distribution, given the O VI column density. This 99^{th} percentile is roughly the 1σ lower limit for the discrepancy with the EAGLE predictions (Fig. 5.5). Therefore, the high O VII column density may not represent a strong tension between the observations and the predictions of EAGLE.

The difference in predicted neighbour distances is less likely to be a selection effect, as we constrained the column densities of all the measured ions to create the sample of EAGLE absorbers, and matched the expected minimum stellar mass for the observed galaxies. The measured absorber is further from its closest neighbours than EAGLE would predict, though only the closest neighbour distance is unlikely enough in EAGLE that it may represent a tension. Ultimately, it is difficult to draw strong conclusions about the validity of the EAGLE model from a single absorption system.

5.5 Discussion

From two of the claimed absorption systems, it seems that EAGLE may under-predict the number of strong O VII absorbers well outside R_{200c} of galaxies. We stress that this is not a certain conclusion, given that we only have two absorption systems for which this seems to be the case, and the detection of one of those is particularly uncertain. However, if EAGLE indeed under-predicts the occurence of such absorbers, there could be a number of issues at play.

If the absorption systems probe the outflows of galaxies detected in the surveys, the EAGLE outflows may not carry enough metals to distances significantly larger than R_{200c}, or the outflows may not be at the right temperature to produce O VII. Alternatively, these absorption systems may probe the CGM or outflows from smaller galaxies, undetected in the surveys and missing in EAGLE due to its limited resolution.

A lack of metals at sufficient densities outside the CGM is, however, somewhat in tension with the reasonable agreement of EAGLE UV metal ion column density distributions (Schaye et al. 2015; Rahmati et al. 2016) to observations. The EAGLE column density distributions represent lower-density structures as well as the CGM (Rahmati et al. 2016; Wijers et al. 2020). In addition, Johnson et al. (2019) searched the 1ES1553+113 FUV spectrum for O VI and H I absorbers, and searched for galaxies in the vicinity of these UV absorbers. Their analysis found that metals are not typically found as far from galaxies as the $z = 0.355$ system claimed by Nicastro et al. (2018). Therefore, FUV observations point to a sufficient amount of dense, metal-enriched gas outside the CGM in EAGLE. However, a dearth of *hot*, dense, metal-enriched gas cannot be excluded based on these UV ion measurements, and the spatial distribution of these metal absorbers may not be correctly predicted by EAGLE.

The number the X-ray absorber(s) found by Nicastro et al. (2018) is consistent with EAGLE predictions. However, the large uncertainties in the inferred absorber density along the line of sight, mostly due to the small number of absorbers, mean that this is more of a sanity check than a stringent test of the EAGLE model.

The X-ray absorbers found as counterparts to O VI absorbers have higher column densities than is typical for such counterparts in EAGLE. However, the relatively high column densities are reasonably consistent with the EAGLE predictions if we also account for the non-detections: the probability of at least one absorber as discrepant as the Ton S 180 absorber is ≈ 0.1–0.2. The probability that at least two of the counterparts have column densities above the 90^{th} (95^{th}) percentiles of the probability distribution for a single UV absorber are 0.3–0.7 (0.1–0.3). The lower (upper) ends of the ranges we give are for 11 (23) trials, reflecting the number of redshifts of O VI absorbers (O VI and broad H I absorbers) searched

for X-ray absorption.

5.6 Summary

Overall, EAGLE seems to hold up reasonably to some of the scarce data available on soft X-ray absorption. There is some indication that the strongest absorbers are clustered too close to galaxies in EAGLE, but this is based on two observations, so it is not a strong tension. These studies and comparisons do illustrate the sorts of information that will become available when instruments with higher sensitivities and spectral resolution increase the number of absorption systems we can measure, and the information we can get for each system. For example, measuring more systems and more ions in each system, will mean we can better measure the temperature, spatial distribution, and mass of the warm-hot CGM and the WHIM.

The measurements we have also make clear that we can learn much more from X-ray absorption spectra when we combine them with other data. For example, the UV spectra provide information on the phase structure of the gas (through absorption from various lower ionization states) and the metallicity of the gas (through H I absorption). Galaxy redshift surveys can tell us whether any absorber represents CGM or filament gas, and more information on those galaxies will be very helpful in understanding the baryon cycle.